

ARTICLE OPEN

Photo-tunable transfer characteristics in MoTe₂–MoS₂ vertical heterostructureArup Kumar Paul¹, Manabendra Kuri¹, Dipankar Saha², Biswanath Chakraborty¹, Santanu Mahapatra², A. K Sood¹ and Anindya Das¹

Fabrication of the out-of-plane atomically sharp p–n junction by stacking two dissimilar two-dimensional materials could lead to new and exciting physical phenomena. The control and tunability of the interlayer carrier transport in these p–n junctions have a potential to exhibit new kind of electronic and optoelectronic devices. In this article, we present the fabrication, electrical, and optoelectrical characterization of vertically stacked few-layers MoTe₂(p)–single-layer MoS₂(n) heterojunction. Over and above the antiambipolar transfer characteristics observed similar to other hetero p–n junction, our experiments reveal a unique feature as a dip in transconductance near the maximum. We further observe that the modulation of the dip in the transconductance depends on the doping concentration of the two-dimensional flakes and also on the power density of the incident light. We also demonstrate high photo-responsivity of $\sim 10^5$ A/W at room temperature for a forward bias of 1.5 V. We explain these new findings based on interlayer recombination rate-dependent semi-classical transport model. We further develop first principles-based atomistic model to explore the charge carrier transport through MoTe₂–MoS₂ heterojunction. The similar dip is also observed in the transmission spectrum when calculated using density functional theory–non-equilibrium Green's function formalism. Our findings may pave the way for better understanding of atomically thin interface physics and device applications.

npj 2D Materials and Applications (2017)1:17 ; doi:10.1038/s41699-017-0017-3

INTRODUCTION

In recent years, van der Waals (vdW) heterostructures based on transition metal dichalcogenides (TMDs) are being studied extensively, due to their excellent electronic and opto-electronic properties^{1–4} with potential applications such as transistor,⁵ photo detector,^{6, 7} light-emitting diode (LED),^{8–10} and solar cells.^{11, 12} Atomically sharp interfaces with intralayer high carrier mobility and lack of dangling bonds result in unique spatial charge separation¹³ between the layers, as well as produce long-lived interlayer excitons¹⁴ under light exposure. These TMD-based vertical heterostructures have shown potentials as p–n junction and most of these p–n junctions show antiambipolar transconductance behavior.^{15–21} However, p–n junction made of single layer of TMDs, known as atomically thin p–n junctions,^{22–25} show quite different type of charge transport mechanism compared to the conventional p–n junction. Here, transport occurs via tunneling of carriers from one layer to the other layer.^{6, 25} This tunneling at the interfaces is predicted to be governed by Shockley-Read-Hall (SRH) or by Langevin recombination mechanisms.²⁵ The band engineering of vertical heterostructures²⁶ with available TMDs having different band gaps and work functions have paved the way to investigate the charge transport mechanisms in atomically thin p–n junction.

In this work, we have carried out electrical and photo-conductivity measurements of vertical heterostructures made of a few-layers MoTe₂ (~6 layers) and single-layer MoS₂. The junction current (I_{DS}) vs. bias (V_{DS}) data show the characteristics of a p–n junction. Interestingly, the I_{DS} as a function of back gate voltage (V_{BG}) show an unusual dip at the highest conductance value on top of the usual antiambipolar nature.^{15–21} We further show that the magnitude and

the position of the dip in I_{DS} – V_{BG} curve can be modulated by changing the incident power density of light. This unique observation can be explained by including interlayer recombination rate of charge carriers along with the individual layer response. We also report very high photo-responsivity of $\sim 10^5$ A/W under forward bias 1.5 V at room temperature. It is seen that the photo-responsivity for blue (450 nm) and red (650 nm) light is few orders of magnitude higher than near infrared (IR) (850 nm) light. We have further carried out first principles-based density functional theory (DFT)- non-equilibrium Green's function (NEGF) calculations, which do capture the evolution of the above mentioned dip.

RESULTS

Experimental results without light

The schematic of the device and the experimental setup are shown in Fig. 1a. Oxidized silicon wafer with 285-nm thick SiO₂ layer was used as a substrate for the heterojunction devices. Few-layer MoTe₂ was exfoliated on the wafer, followed by transfer of a single-layer MoS₂ flake using well-known polydimethylsiloxane (PDMS) dry transfer technique.²⁷ The metal contacts on individual flakes were made using standard e-beam lithography, followed by thermal deposition of Ti/Au contacts (5/70 nm). For the electrical measurements, DC bias (V_{DS}) was applied and the output current (I_{DS}) was measured with a current amplifier as shown in Fig. 1a. In order to change the carrier concentration, the gate voltage (V_{BG}) was applied to the P^{++} Si substrate. The fabrication details as well as measurement details have been mentioned in the "Methods" section. Figure 1b shows the optical as well as atomic force microscope (AFM) image of one of the devices, termed as D1. As

¹Department of Physics, Indian Institute of Science, Bangalore 560012, India and ²Department of Electronic Systems Engineering, Indian Institute of Science, Bangalore 560012, India

Correspondence: Anindya Das (dasanindy@gmail.com)

Received: 9 December 2016 Revised: 25 May 2017 Accepted: 30 May 2017

Published online: 27 June 2017

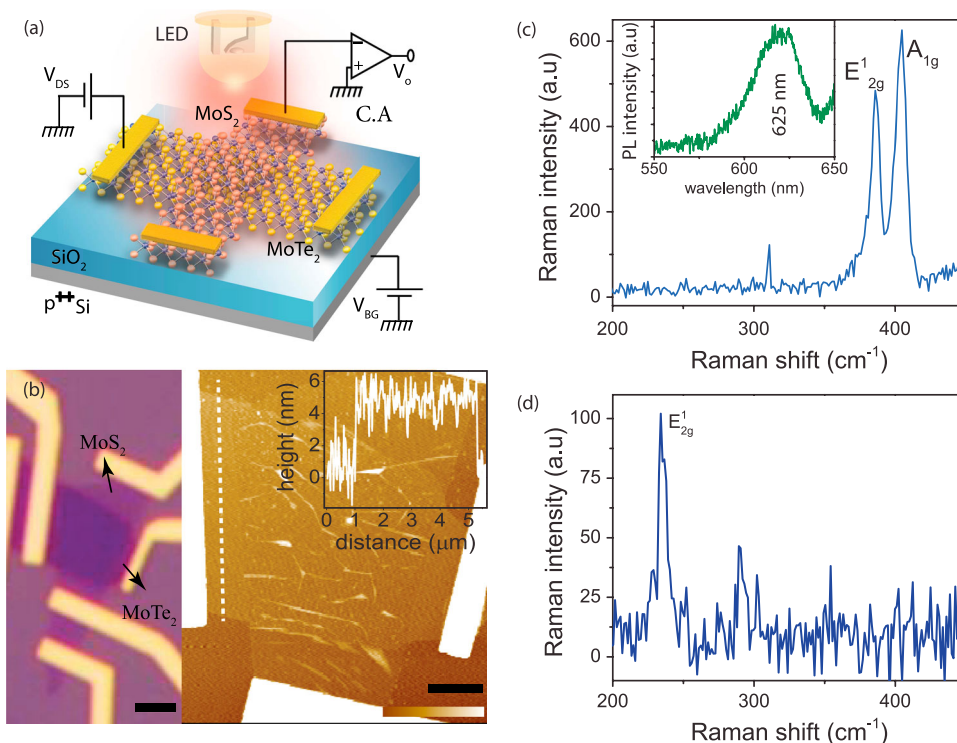


Fig. 1 **a** Schematics of the device, with the experimental setup. Bias (V_{DS}) was applied to MoTe₂ flake and current output was measured with a current amplifier (CA) connected to MoS₂ flake. Gate voltage (V_{BG}) was applied to P⁺⁺ Si of the substrate. LED was used to illuminate the sample for opto-electronics measurements. **b** Optical image (left) and AFM image (right) of the device. The scale bar (black) for optical and AFM images are, respectively, 2 μm and 1 μm . The color scale bar for AFM image is 85 nm. Inset is MoTe₂ height profile along the dashed line. **c** Raman and PL (inset) of MoS₂. **d** Raman for MoTe₂

seen in Fig. 1b, the measured height of the MoTe₂ flake was 4 nm, corresponding to six layers.^{28, 29} Figure 1d depicts the Raman spectra of the MoTe₂ flake, which shows the characteristic in plane E_{2g}^1 peak at 234 cm^{-1} .^{24–29} The Raman spectra for MoS₂ flake is shown in Fig. 1c. Here, the MoS₂ characteristic E_{2g}^1 and out of plane A_{2g} peaks can be seen, respectively, at 386 and 405 cm^{-1} . The inset of Fig. 1c shows the MoS₂ photoluminescence (PL) spectra, which shows a single peak near 625 nm. Both Raman and PL verifies that the MoS₂ flake is a single layer.^{30, 31}

Electrical and opto-electronic measurements were performed at room temperature in a vacuum of 10^{-5} mbar on seven devices. Though the responses were similar in all the devices, the magnitude of the response varied from sample to sample, depending on the quality of the contacts as well as the quality of the heterojunction interface. Here, we discuss four devices, for which best results were obtained. Figure 2a shows conductance (G) as a function of V_{BG} for individual MoS₂ (red curve) and MoTe₂ (blue curve) for the D1 device. As can be seen in Fig. 2a, MoS₂ flake is n-doped with a threshold voltage (V_{th}) ~ -20 V and MoTe₂ flake is p-doped with $V_{th} \sim +5$ V. The $I_{DS}-V_{DS}$ response of individual flakes, shown in the Supplementary Information (SI), indicates absence of any significant Schottky barriers at the contacts. Figure 2b displays the $I_{DS}-V_{DS}$ response of the junction for several V_{BG} , showing rectification behavior, expected for the p-n junction at the interface. Even though the observed $I_{DS}-V_{DS}$ curve is qualitatively similar to a conventional p-n junction, the current does not increase exponentially with forward bias; rather, it increases almost linearly, pointing to the underlying rectification mechanism being different.²⁵ The $I_{DS}-V_{BG}$ plots for different V_{DS} are shown in Fig. 2c. The overall antiambipolar shape of the curves can be understood qualitatively by considering the resistances of MoS₂ and MoTe₂ parts in series. At large positive V_{BG} ($V_{BG} > 20$ V) and negative V_{BG} ($V_{BG} < -20$ V) the current is very small, as one of

the layer goes to the insulating state. The current is maximum near $V_{BG} \sim -10$ V, as expected from the conductance of individual layers seen in Fig. 2a. Though this series resistance model is able to explain the antiambipolar nature of the transconductance, it is inadequate to explain the unusual dip near the conductance maximum near -10 V. Inset of Fig. 2c shows the $I_{DS}-V_{BG}$ response from yet another device (D2), which also shows similar dip near the conductance maximum ($V_{BG} \sim -13$ V). However, for D3 and D4 devices (Fig. 2d) no dip was observed. In the next paragraph we will show that the dip can be tailored with the incident light. The detailed characteristics of these devices are given in SI.

Experimental results with light

To further elucidate the $I_{DS}-V_{BG}$ curves, we have carried out the transport measurements with the exposure of light for blue (wavelength $\lambda \sim 450$ nm), red ($\lambda \sim 650$ nm), and near IR ($\lambda \sim 850$ nm) LEDs on the D3 device. It was observed that the device response changed drastically with exposure of light, and even after LED was switched off the changes were retained for a long time ~ 24 h. First, $I_{DS}-V_{BG}$ measurements are made as a function of incident light intensity (in increasing order), and then with the light off gate response is measured at regular intervals of time for several hours until the response curve is same as the initial state. Similar results were obtained in repeated runs of light-on/light-off cycles. Figure 3a shows the evolution of the gate response (at $V_{DS} = 1.5$ V) under blue LED for the second cycle of measurements. It can be seen that with increasing light intensity the peak value of I_{DS} increases and the position of the peak systematically shifts toward higher negative gate voltages. This shift of position (ΔV_{BG}) of peak I_{DS} as a function of power density is shown in Fig. 3d (green curve). As can be seen in Fig. 3a, the V_{th} on the left side of the peak moves toward more negative V_{BG} without affecting significantly the V_{th} on the right side. This suggests that with increasing light intensity the MoS₂ flake gets

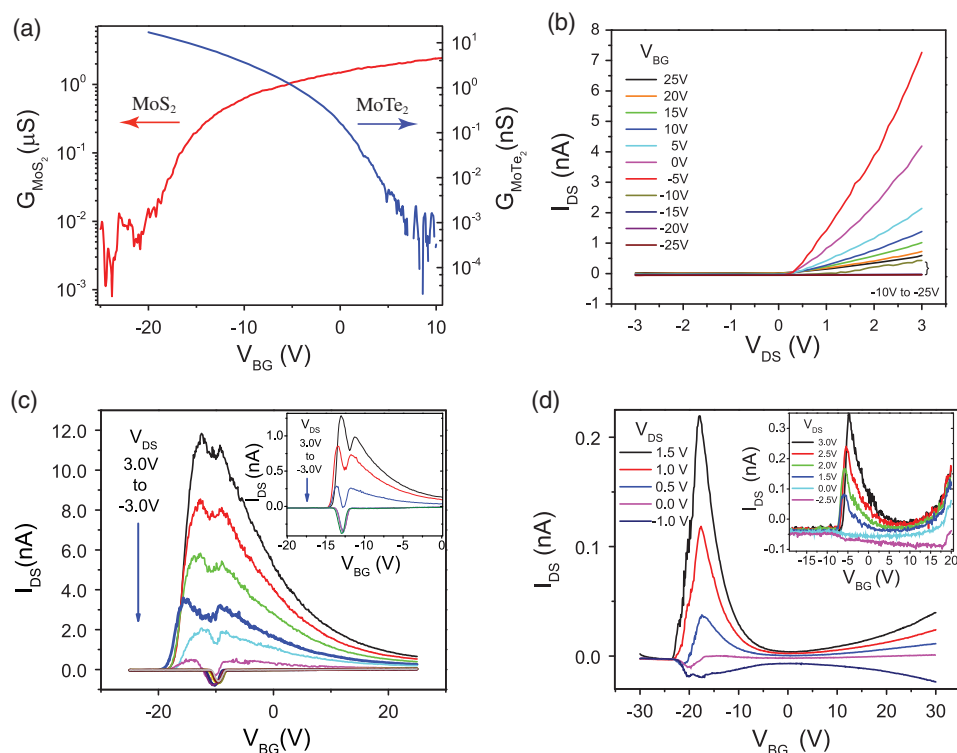


Fig. 2 **a** Gate response of individual MoS₂ (red curve) and MoTe₂ (blue curve) for device D1. **b** I_{DS} - V_{DS} response of the junction. Responses for $V_{BG} -20$ V to -5 V shows clear rectification behavior. **c** I_{DS} - V_{BG} response of the junction for $V_{DS} -3$ V to $+3$ V in 0.5 V steps. An anomalous dip can be observed near the maximum of current in forward bias. *Inset* shows I_{DS} - V_{BG} response for device D2. Here also similar dip can be observed. **d** I_{DS} - V_{BG} response for device D3 and *inset* shows the same for device D4. No dip was observed for D3 and D4

more n-doped, while the change in MoTe₂ doping is very small. Most interestingly, the dip in gate response curve near the maximum I_{DS} starts appearing with increasing optical power and then vanishes at higher light intensities. In the *inset* of Fig. 3a, we show gate response for three different light intensities during the first cycle of the measurement. The magnitude of the dip (ΔI_{DIP}) as a function of power density is plotted in Fig. 3d (blue curve). A comparison of I_{DS} - V_{DS} characteristics under dark and illuminated condition at $V_{BG} = -30$ V has been shown in Fig. 3b. The overall I_{DS} - V_{DS} curve under illumination is similar to that of the device in on-state (SI). It may be noted that the device goes from completely off-state to on-state with light. This behavior could be understood as following: at $V_{BG} = -30$ V the junction does not conduct in dark state because MoS₂ is completely depleted and starts conducting on light exposure, as MoS₂ gets doped. *Inset* of Fig. 3b shows the response of the device (at $V_{DS} = 1$ V, $V_{BG} = -30$ V) to a very short light pulse. Though switching time from off to on state is less than ~ 600 ms (limited by our measuring instrument), the device shows a strong memory effect as I_{DS} reduces slowly with time. In Fig. 3c, the evolution of gate response with time is shown after the LED was switched off (LED off part of the second cycle) and it takes almost a day for the response to come back to its initial condition. Interestingly, here also we see the dip appearing and again disappearing with time. The quantitative measure of ΔI_{DIP} with time has been plotted in Fig. 3e.

Photo-responsivity

Similar to the results for blue LED shown in Fig. 3, the experiments were performed with red and IR LEDs. The overall transconductance behavior of the device was similar, except for the magnitude of I_{DS} , for all the LEDs, as shown in Fig. 4a. I_{ph} is taken as the difference of I_{peak} of the gate response under illumination to the corresponding I_{DS} in gate response without illumination. As shown in Fig. 4a, I_{ph} is maximum for the red light. In SI Fig. S5 I_{DS} - V_{DS} responses under dark and illuminated condition has been

compared for several V_{BG} , which shows the dependence of photo-responsivity on V_{DS} . The highest photo response is achieved at $V_{DS} = 1.5$ V, which has been plotted in Fig. 4b. The nature of plots is very similar to MoS₂-graphene heterostructures.³² As can be seen, for red and blue light, photo-responsivity $\sim 10^5$ A/W has been achieved. For IR light (1.45 eV), the photo-responsivity is several orders of smaller (Fig. 4b) as the photon energy is below the band gap of single-layer MoS₂.

DISCUSSION

Understanding the dip in photo response within a classical model We use the interlayer recombination model²⁵ to understand the results presented in Fig. 3. Under forward bias the charge carriers conduct via tunneling-mediated interlayer recombination as $I_{DS} \propto R_C V_{DS}$, where R_C is the recombination rate. R_C is proportional to n_{eff}/τ , where n_{eff} is effective carrier concentration and τ is interlayer tunneling time. Here, $n_{eff} = n_S p_T / (n_S + p_T)$, where n_S and p_T are the electron and hole concentrations of individual flakes, which are tuned by gate voltage as well as light intensity. In Fig. 5, the effect of photo-doping on R_C has been discussed. Here, we have used the SRH mechanism for R_C .²⁵ However, similar kind of transport characteristics can be obtained from Langevin processes.²⁵ The photo-induced doping mechanism has been illustrated schematically in Fig. 5a, where the gate voltage drops mostly across the SiO₂ layer and few-layers MoTe₂. The incident photons create electron-hole pairs in both MoS₂ and MoTe₂, but due to the presence of electric field (negative V_{BG}) the excited electrons (holes) will move toward the MoS₂ layer (MoTe₂-SiO₂ interface), moving the Fermi level in MoS₂ closer to the conduction band (Fig. 5a). However, the photo-excited holes in MoTe₂ get trapped mostly at the MoTe₂-SiO₂ interface as well as at the defect states inside the MoTe₂ closer to its valence band, which are mostly immobile (reflected in poor mobility < 1 cm²/Vs)

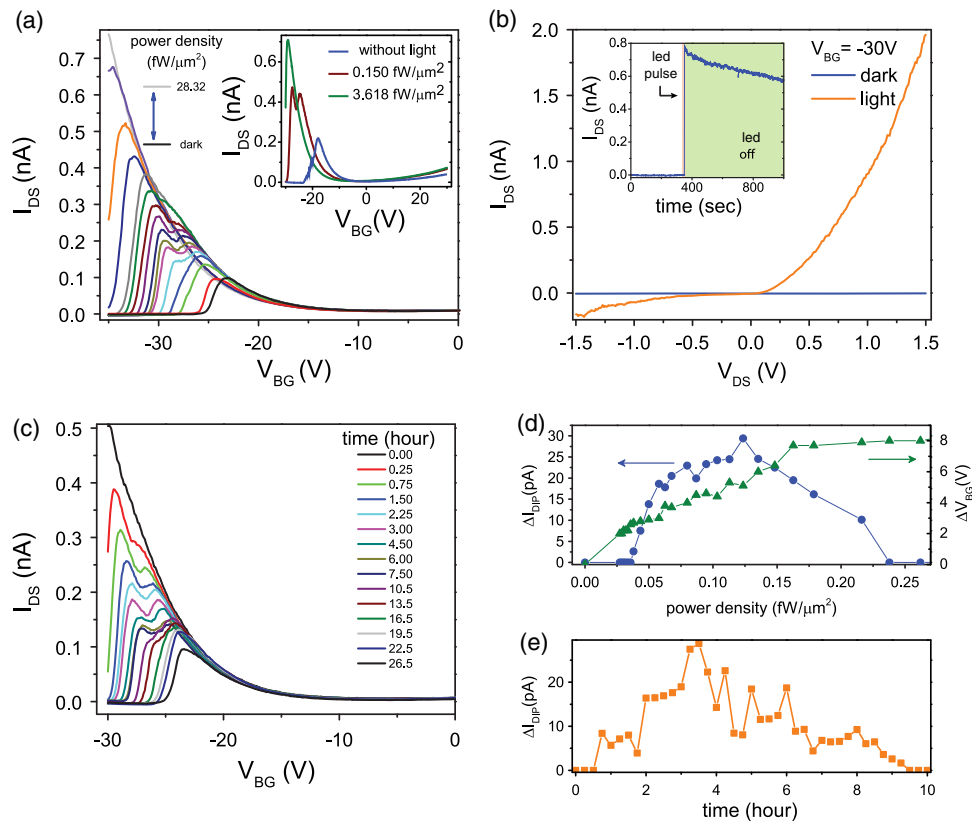


Fig. 3 **a** Evolution of I_{DS} - V_{BG} response of device $D3$, with increasing light intensity (blue) during second cycle. The dip can be seen appearing and again disappearing with increasing optical power. *Inset* shows evolution of I_{DS} - V_{BG} during first cycle. **b** Comparison of I_{DS} - V_{DS} response under dark and illuminated condition. *Inset* shows led pulse experiment, which shows memory effect. **c** Evolution of I_{DS} - V_{BG} with time after led was switched off. Here also the dip can be seen appearing after few hours, and then again vanishing. **d**, **e** Evolution of dip magnitude (ΔI_{DIP}) with optical power density and time

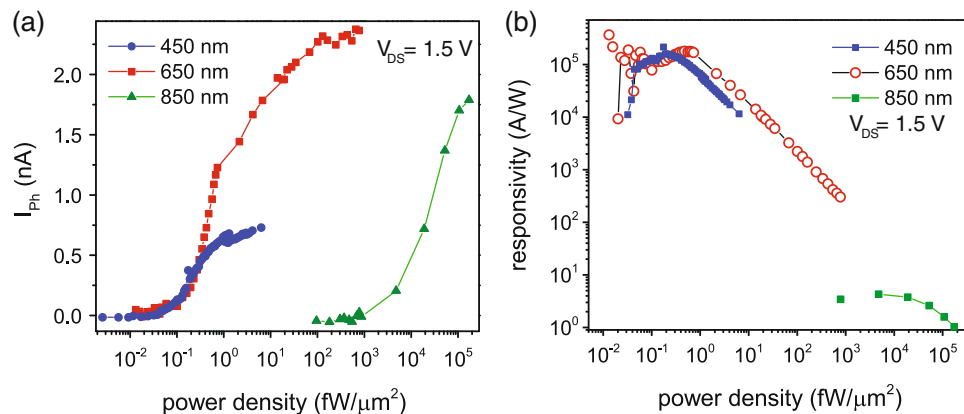


Fig. 4 For device $D3$. **a** Photo current (I_{ph}) as function of optical power density for red (red curve), blue (blue curve), and IR (green curve) LEDs. **b** Photo-responsivity for red, blue, and IR light at $V_{DS} = 1.5$ V. Though for red and blue the photo-responsivity was similar and of the order of 10^5 A/W, for IR it is several orders of magnitude small

and hence do not participate in conduction.^{32–35} This also explains why it takes almost a day to come back to its initial value after the light is off (Fig. 3c). The photo-induced effect has been quantitatively presented in Fig. 5b. The induced carrier concentration (n) as a function of V_{BG} in MoS_2 and MoTe_2 has been generated using capacitive model, $n = n_0 + C_G(V_{BG} - V_{th})/e$, where C_G is the geometrical capacitance and n_0 is the majority carrier concentration due to trap and defect states for $V_{BG} < V_{th}$. In this model, we have taken $n_0 = 3 \times 10^{13} \text{ m}^{-2}$, which is similar to ref. 25. With increasing optical power density we have shifted the V_{th} of

MoS_2 toward left side by ΔV_{BG} comparable to the experimental values (Fig. 3d). To explain the transconductance data of our device in Fig. 3, we need to consider resistances coming from both the individual layers (non-overlapped) as well as the junction part (overlapped). However, the gate response of the individual flakes (non-overlapped) changes less significantly with light (see SI), and hence we consider only the effect of the junction. In the *bottom panel* of Fig. 5b, we have plotted R_C as a function of V_{BG} for different amount of photo-induced doping as shown in Fig. 5b (*upper panel*). This classical model qualitatively shows the

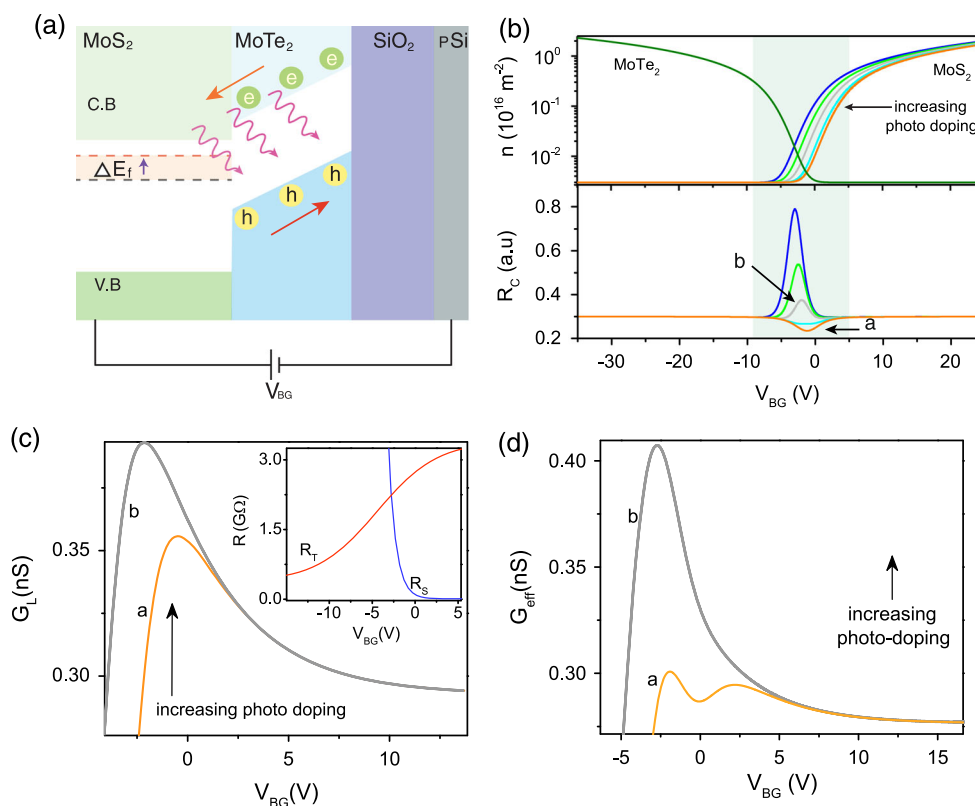


Fig. 5 **a** Schematic diagram of photo-induced doping process of MoS₂ and MoTe₂ flakes. **b** Capacitive model to simulate effect of photo doping on the carrier concentration of individual flakes. *Upper panel* shows carrier concentration (n) vs. V_{BG} plot for both flakes. For MoS₂, n - V_{BG} curves with different V_{th} has been plotted considering its pronounced photo-doping effect. On the other hand, one fixed n - V_{BG} has been plotted for MoTe₂, as it shows much less photo-doping effect. In the *lower panel*, R_c - V_{BG} graphs has been plotted for the corresponding MoS₂ n - V_{BG} curves. The curves marked by “a” and “b” are used for G_{eff} calculation. **c** G_L as function of V_{BG} for two different V_{th} of MoS₂ corresponding to the “a” and “b” n - V_{BG} curves. *Inset* shows the individual resistance R_S and R_T as functions of V_{BG} . **d** G_{eff} as function of V_{BG} . As can be seen G_{eff} captures the dip to peak transition

transformation from a dip to no-dip in the modulation of recombination rate by the photo-induced doping.

To understand how R_c influences the overall transconductance curve, we need to consider the lateral series resistance (R_L) coming from the individual flakes at junction, as well as the tunneling resistance (R_j), which is inversely proportional to R_c . R_L is equal to $R_S + R_T$, where R_S and R_T are lateral resistances coming from individual MoS₂ and MoTe₂, respectively. In Fig. 5c, the *inset* shows R_S and R_T as functions of V_{BG} . These have been obtained by fitting the experimental G - V_{BG} curve of MoS₂ and MoTe₂, respectively (for device D3). Figure 5c shows the plot of total lead conductance $G_L = (R_S + R_T)^{-1}$ vs. V_{BG} for two different V_{th} of MoS₂ (differing by $\Delta V_{BG} \sim 2.5$ V) corresponding to the curves marked by “a” and “b” in Fig. 5b (*lower panel*). Please note that Fig. 5c does not capture the dip observed in our experiments. Next, we show the effect on the transconductance by including the series resistance R_L along with the tunneling resistance R_j . In Fig. 5d, we plot $G_{eff} = (R_L + R_j)^{-1}$ as a function V_{BG} corresponding to the same “a” and “b” curves in Fig. 5b. It can be seen that the dip can be qualitatively explained by inclusion of the interlayer recombination rate.

DFT-NEGF calculation

In order to get insights on the charge carrier transport through MoTe₂-MoS₂ vdW interface, we have also carried out an atomistic study³⁶⁻⁴¹ on the two port device structures as illustrated in Fig. 6. As shown in Fig. 6a, the length of the channel region (L) is taken as ~ 6.6 nm (along the transport direction, i.e., the Z-axis), whereas the MoS₂-MoTe₂ overlapping distance is maintained as ~ 2.2 nm (which is 1/3rd of the total channel length). Moreover, along the X-axis

(perpendicular to the plane) we incorporate a vacuum region of 15 Å (sufficient to avoid any spurious interaction between periodic images). Here, the left ($t_{left} \sim 16.57$ Å) and the right ($t_{right} \sim 16.57$ Å) electrodes are acting as the semi-infinite reservoirs. Here, after we will call this device structure as vdW interface1. Besides, the zoomed region shown within dotted arrows portrays the top view of the channel of MoS₂-MoTe₂ vdW interface (having an width ~ 1 nm). The details of the calculation are given in the SI.

Next, we consider two more variants of the aforementioned device (namely, vdW interface2 and vdW interface3), where the MoS₂ and the MoTe₂ flakes are of doped with different doping concentrations. In ATK (Atomistix Tool Kit), the effective doping (n-type or p-type) can be achieved by means of incorporating appropriate compensation charge to the system.^{42, 43} This effective doping scheme (atomic compensation charge) is really advantageous, as it does not depend either on the exact dimensions of the system or on the specific details of the dopant atoms.⁴² Considering moderate and high doping densities $3.85 \times 10^{17} \text{ cm}^{-3}$ and $1.28 \times 10^{19} \text{ cm}^{-3}$, we set the “atomic compensation charge” values,⁴⁴ which are equivalent to two-dimensional densities $2.56 \times 10^{14} \text{ m}^{-2}$ and $8.5 \times 10^{15} \text{ m}^{-2}$, respectively. For vdW interface2 and vdW interface3, the MoS₂ flakes are n-doped, whereas the MoTe₂ flakes are p-doped, with the corresponding “atomic compensation charge” values. It is important to realize that, for any DFT-NEGF simulation, the electrodes act as the carrier reservoirs to maintain equilibrium for the entire system.⁴² Moreover, taking vdW interface3 into consideration, we find that the energy-position resolved local density of states (LDOS) diagram (as shown in Fig. 6) clearly represents the band alignment of a type-II heterostructure.

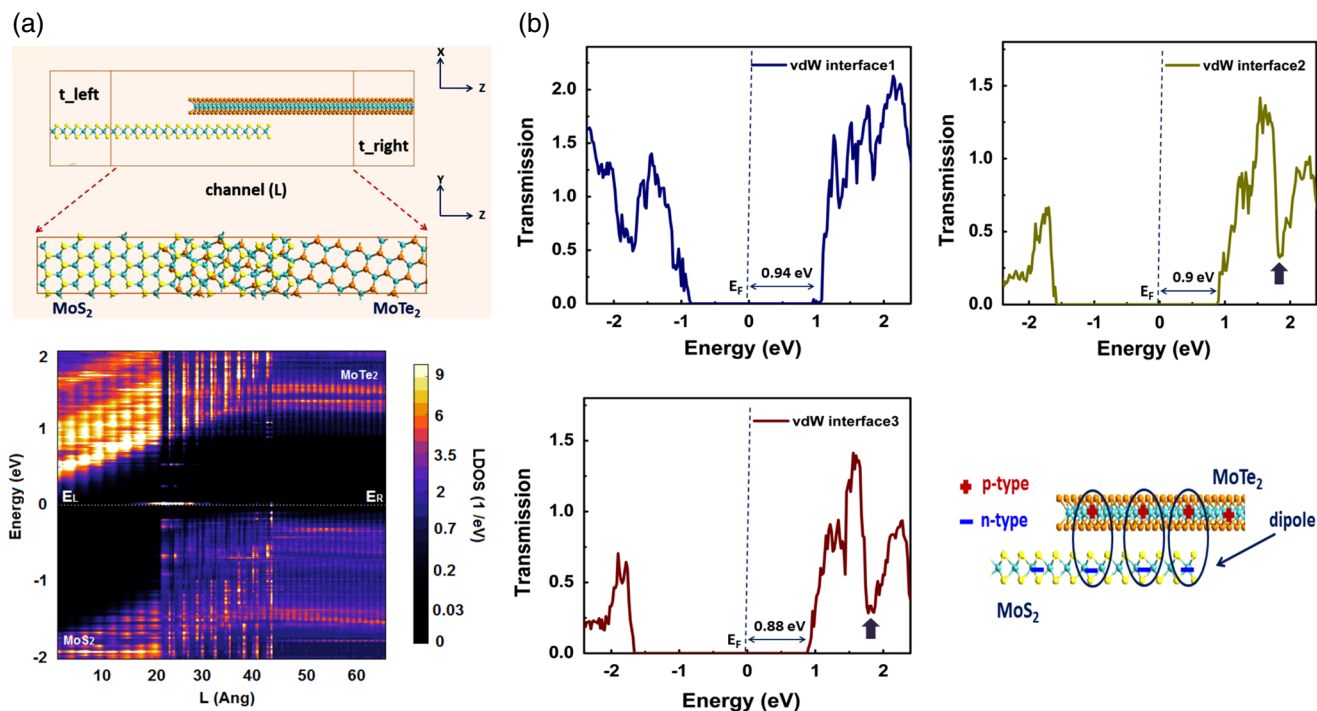


Fig. 6 **a** (top) MoTe₂-MoS₂ vdW interface, where length of the channel is ~ 6.6 nm and width is ~ 1 nm. (bottom) Energy-position resolved LDOS diagram for the vdW interface3. **b** Transmission spectra of vdW interface1 (upper left), vdW interface2 (upper right), and vdW interface3 (bottom left). (bottom right) The schematic illustrates the formation of electric dipoles along the channel

Figure 6b illustrates the zero bias transmission spectra of the MoS₂-MoTe₂ vdW interfaces. It is quite interesting to observe that the transmission spectra obtained for the vdW interface2 and vdW interface3 structures are quite different from that of the vdW interface1. For the intrinsically charge neutralized MoS₂ and MoTe₂ sheets of vdW interface1, we see no significant dip states, within the positive energy range of 0 to 2 eV. However, for the samples those are effectively doped into n-type and p-type, we notice the distinct effect of charge separation. The excess negative and positive charge carriers across the individual layers (Fig. 6b, bottom right) give rise to strong interlayer coupling and modulates the transmission states within the range of 0–2 eV. Here, we emphasize on the positive energy transmission states of the individual vdW interfaces. It is worth mentioning that for near-equilibrium electrical current calculation, the states within the bias window ultimately matters. So for any finite bias, the states that are closer to the Fermi energy (E_F) will play the dominant role. Nonetheless, it can be seen from Fig. 6b that the states corresponding to $V.B_{max}$ have further been shifted away from the energy zero (i.e., $E-E_F=0$) for the vdW interface2 and the vdW interface3. Considering the energy range of 0–2 eV, it is evident from Fig. 6b (upper left) that there will be no anomalous dip in the maximum current (at forward bias) for the vdW interface1. However, this is not the same for other device(s) with excess n-type or p-type carriers. Investigating the transmission spectra, as illustrated in Fig. 6b (upper right and bottom left), we observe clear dips (pointed by arrows) around 1.8 eV. A quantitative calculation of transmission spectra as a function of back gate voltage is, however, beyond the scope of our work at this stage.

To understand the physics behind the atypical nature of the transmission spectra obtained for vdW interface2 and vdW interface3, we propose a plausible explanation. It is known from the literature¹³ that the excess negative and positive charge carriers across the individual layers (Fig. 6b) make interlayer electric dipoles, which could be the permanent one.^{13, 14, 45} Nevertheless, this will give rise to a strong interlayer coupling, and perhaps shift-in the trenches of the transmission spectra to the

lower-energy range values (which is ~ 1.8 eV, in this case). Even though both classical and DFT-NEGF calculations qualitatively support our observation, a complete understanding of the transformation of the dip need further theoretical work.

In summary, we demonstrate electrical and opto-electronic measurements on MoTe₂-MoS₂ vdW heterojunction devices. In normal transconductance measurements, some of the devices showed an anomalous dip in current near the maximum conductance state. We showed that the dip can be modulated with light intensity. We have correlated this anomalous feature within a classical model based on interlayer recombination processes, followed by electrical transport calculations using DFT-NEGF. The first principles-based quantum transport calculation qualitatively capture the anomalous feature depending on the carrier concentration of the individual flakes. Our devices also show large photo response of $\sim 10^5$ A/W at room temperature, which makes it a potential candidate for charge integrating type opto-electronic applications.

METHODS

The heterojunction devices were fabricated on Si/SiO₂ substrate with 285-nm thick SiO₂ layer. The MoS₂ and MoTe₂ flakes were exfoliated on PDMS and substrate, respectively, from bulk crystal using scotch tape method. To make heterojunction devices, the thinnest flakes were identified with optical microscope. Then Raman and PL spectroscopy was used to sort out single-layer MoS₂ and non-contact AFM was used to identify 6–8 layers of MoTe₂ flakes. All the AFM characterizations were performed with Park NX10 AFM. After transferring the MoS₂ flakes on the MoTe₂ flakes, the electrical contacts were patterned using standard e-beam lithography. Then Ti/Au (5/70 nm) were deposited on the lithography-patterned sample, by thermal evaporation to realize the electrical contacts. The electrical and opto-electronic measurements were performed inside a home-built cryostat, under vacuum of 10^{-5} mbar at room temperature. For all DC characterization, Keithly 2400 source-meter, Agilent 34401A digital multimeter, and a home-built low-noise current amplifier was used. For opto-electrical measurements, the leds were fixed at ~ 2 mm distance from the devices. The leds were illuminated with Keithly 2400 in current source mode. The led power was calibrated with PM203 Thorlabs optical power meter.

Data availability

The authors declare that the main data supporting the findings of this study are available within the paper and its SI file. Other relevant data are available from the corresponding author upon request.

ACKNOWLEDGEMENTS

The device fabrication was performed using facilities at CeNSE, funded by Department of Information Technology, Govt. of India, and located at Indian Institute of Science, Bangalore. A.K.S. thanks Department of Science and Technology (DST), India for financial support. A.D. thanks DST and Indian Space Research Organization (ISRO) for financial support. This work is supported by Department of Science and Technology (DST), Government of India, under Grant No: DSTO/PPH/AYD/1470, and Indian Space Research Organization (ISRO), Government of India, under Grant No: ISTC/PPH/AYD/0343. S.M. acknowledges the support by Science and Engineering Research Board (SERB), Department of Science and Technology (DST), Government of India, under Grant No: SB/S3/EECE/0209/2015.

AUTHOR CONTRIBUTIONS

A.P., A.K.S., and A.D. conceived the idea of this research. A.D. and A.P. together designed the experimental setup. A.P. performed the heterojunction device fabrication, electrical and opto-electronic characterization of the heterojunctions, and data analysis. M.K. optimized the transfer technique. B.C. did the Raman and PI characterizations. D.S. and S.M. developed the atomistic device model and performed the DFT-NEFG calculations. All author contributed in writing the manuscript.

ADDITIONAL INFORMATION

Supplementary Information accompanies the paper on the *npj 2D Materials and Applications* website (doi:10.1038/s41699-017-0017-3).

Competing interests: The authors declare no competing financial interests.

Publisher's note: Springer Nature remains neutral with regard to jurisdictional claims in published maps and institutional affiliations.

REFERENCES

- Novoselov, K., Mishchenko, A., Carvalho, A. & Neto, A. C. 2D materials and van der Waals heterostructures. *Science* **353**, aac9439 (2016).
- Das, S., Robinson, J. A., Dubey, M., Terrones, H. & Terrones, M. Beyond graphene: progress in novel two-dimensional materials and van der Waals solids. *Ann. Rev. Mater. Res.* **45**, 1–27 (2015).
- Jariwala, D., Marks, T. J. & Hersam, M. C. Mixed-dimensional van der Waals heterostructures. *Nat. Mater.* **16**, 170–181 (2016).
- Bablich, A., Kataria, S. & Lemme, M. C. Graphene and two-dimensional materials for optoelectronic applications. *Electronics* **5**, 13 (2016).
- Roy, T. et al. Dual-gated MoS₂/WSe₂ van der Waals tunnel diodes and transistors. *ACS Nano* **9**, 2071–2079 (2015).
- Zhang, K. et al. Interlayer transition and infrared photodetection in atomically thin type-II MoTe₂/MoS₂ van der Waals heterostructures. *ACS Nano* **10**, 3852–3858 (2016).
- Li, Y., Xu, C.-Y., Wang, J.-Y. & Zhen, L. Photodiode-like behavior and excellent photoresponse of vertical Si/monolayer MoS₂ heterostructures. *Sci. Rep.* **4**, 17186 (2014).
- Withers, F. et al. Light-emitting diodes by band-structure engineering in van der Waals heterostructures. *Nat. Mater.* **14**, 301–306 (2015).
- Ross, J. S. et al. Electrically tunable excitonic light-emitting diodes based on monolayer WSe₂ pn junctions. *Nat. Nanotechnol.* **9**, 268–272 (2014).
- Withers, F. et al. WSe₂ light-emitting tunneling transistors with enhanced brightness at room temperature. *Nano Lett.* **15**, 8223–8228 (2015).
- Flöry, N. et al. A WSe₂/MoSe₂ heterostructure photovoltaic device. *Appl. Phys. Lett.* **107**, 123106 (2015).
- Furchi, M. M., Pospischil, A., Libisch, F., Burgdölfler, J. & Mueller, T. Photovoltaic effect in an electrically tunable van der Waals heterojunction. *Nano Lett.* **14**, 4785–4791 (2014).
- Fogler, M., Butov, L. & Novoselov, K. High-temperature superfluidity with indirect excitons in van der Waals heterostructures. *Nat. Commun.* **5**, 4555 (2014).
- Rivera, P. et al. Observation of long-lived interlayer excitons in monolayer MoSe₂-WSe₂ heterostructures. *Nat. Commun.* **6**, 6242 (2015).
- Jariwala, D. et al. Hybrid, gate-tunable, van der Waals p-n heterojunctions from pentacene and MoS₂. *Nano Lett.* **16**, 497–503 (2015).
- Jariwala, D. et al. Large-area, low-voltage, antiambipolar heterojunctions from solution-processed semiconductors. *Nano Lett.* **15**, 416–421 (2014).

- Yi, S.-G. et al. Optoelectric properties of gate-tunable MoS₂/WSe₂ heterojunction. *IEEE Trans. Nanotechnol.* **15**, 499–505 (2016).
- Wang, Z., He, X., Zhang, X.-X. & Alshareef, H. N. Hybrid van der Waals p-n heterojunctions based on SnO and 2D MoS₂. *Adv. Mater.* **28**, 9133–9141 (2016).
- Li, Y. et al. Anti-ambipolar field-effect transistors based on few-layer 2D transition metal dichalcogenides. *ACS Appl. Mater. Interfaces* **8**, 15574–15581 (2016).
- Jariwala, D. et al. Gate-tunable carbon nanotube–MoS₂ heterojunction pn diode. *Proc. Natl. Acad. Sci.* **110**, 18076–18080 (2013).
- Kim, J.-K. et al. Trap-mediated electronic transport properties of gate-tunable pentacene/MoS₂ pn heterojunction diodes. *Sci. Rep.* **6**, 36775 (2016).
- Cheng, R. et al. Electroluminescence and photocurrent generation from atomically sharp WSe₂/MoS₂ heterojunction p-n diodes. *Nano Lett.* **14**, 5590–5597 (2014).
- Deng, Y. et al. Black phosphorus–monolayer MoS₂ van der Waals heterojunction p-n diode. *ACS Nano* **8**, 8292–8299 (2014).
- Pezeshki, A., Shokouh, S. H. H., Nazari, T., Oh, K. & Im, S. Electric and photovoltaic behavior of a few-layer α-MoTe₂/MoS₂ dichalcogenide heterojunction. *Adv. Mater.* **28**, 3216–3222 (2016).
- Lee, C.-H. et al. Atomically thin p-n junctions with van der Waals heterointerfaces. *Nat. Nanotechnol.* **9**, 676–681 (2014).
- Kang, J., Tongay, S., Zhou, J., Li, J. & Wu, J. Band offsets and heterostructures of two-dimensional semiconductors. *Appl. Phys. Lett.* **102**, 012111 (2013).
- Castellanos-Gomez, A. et al. Deterministic transfer of two-dimensional materials by all-dry viscoelastic stamping. *2D Materials* **1**, 011002 (2014).
- Pradhan, N. R. et al. Field-effect transistors based on few-layered α-MoTe₂. *ACS Nano* **8**, 5911–5920 (2014).
- Lin, Y.-F. et al. Ambipolar MoTe₂ transistors and their applications in logic circuits. *Adv. Mater.* **26**, 3263–3269 (2014).
- Yin, Z. et al. Single-layer MoS₂ phototransistors. *ACS Nano* **6**, 74–80 (2011).
- Late, D. J., Liu, B., Matte, H. R., Dravid, V. P. & Rao, C. Hysteresis in single-layer MoS₂ field effect transistors. *ACS Nano* **6**, 5635–5641 (2012).
- Roy, K. et al. Graphene-MoS₂ hybrid structures for multifunctional photo-responsive memory devices. *Nat. Nanotechnol.* **8**, 826–830 (2013).
- Li, X. et al. Persistent photoconductivity in two-dimensional Mo_{1-x}W_xSe₂-MoSe₂ van der Waals heterojunctions. *J. Mater. Res.* **31**, 923–930 (2016).
- Wu, Y.-C. et al. Extrinsic origin of persistent photoconductivity in monolayer MoS₂ field effect transistors. *Sci. Rep.* **5**, 11472 (2015).
- Li, T., Du, G., Zhang, B. & Zeng, Z. Scaling behavior of hysteresis in multilayer MoS₂ field effect transistors. *Appl. Phys. Lett.* **105**, 093107 (2014).
- Atomistix ToolKit (ATK) with Virtual NanoLab, Version 2015.1, Last accessed_Dec 2016, QuantumWise A/S, <http://quantumwise.com/>.
- Perdew, J. P., Burke, K. & Ernzerhof, M. Generalized gradient approximation made simple. *Phys. Rev. Lett.* **77**, 3865 (1996).
- Ozaki, T. Variationally optimized atomic orbitals for large-scale electronic structures. *Phys. Rev. B* **67**, 155108 (2003).
- Ozaki, T. & Kino, H. Numerical atomic basis orbitals from h to kr. *Phys. Rev. B* **69**, 195113 (2004).
- Grimme, S. Semiempirical GGA-type density functional constructed with a long-range dispersion correction. *J. Comput. Chem.* **27**, 1787–1799 (2006).
- Brandbyge, M., Mozos, J.-L., Ordejón, P., Taylor, J. & Stokbro, K. Density-functional method for nonequilibrium electron transport. *Phys. Rev. B* **65**, 165401 (2002).
- Stradi, D., Martinez, U., Blom, A., Brandbyge, M. & Stokbro, K. General atomistic approach for modeling metal-semiconductor interfaces using density functional theory and nonequilibrium Green's function. *Phys. Rev. B* **93**, 155302 (2016).
- Soler, J. M. et al. The SIESTA method for ab initio order-n materials simulation. *J. Phys. Condens. Matter* **14**, 2745 (2002).
- Zhang, Y. et al. Thickness considerations of two-dimensional layered semiconductors for transistor applications. *Sci. Rep.* **6**, 29615 (2016).
- Yu, Y. et al. Equally efficient interlayer exciton relaxation and improved absorption in epitaxial and nonepitaxial MoS₂/WS₂ heterostructures. *Nano Lett.* **15**, 486–491 (2014).



Open Access This article is licensed under a Creative Commons Attribution 4.0 International License, which permits use, sharing, adaptation, distribution and reproduction in any medium or format, as long as you give appropriate credit to the original author(s) and the source, provide a link to the Creative Commons license, and indicate if changes were made. The images or other third party material in this article are included in the article's Creative Commons license, unless indicated otherwise in a credit line to the material. If material is not included in the article's Creative Commons license and your intended use is not permitted by statutory regulation or exceeds the permitted use, you will need to obtain permission directly from the copyright holder. To view a copy of this license, visit <http://creativecommons.org/licenses/by/4.0/>.

© The Author(s) 2017